Complex magnetic phase diagram in Ce$_3$Pd$_6$Sb$_5$ with a well-ordered superstructure

W. Xie, M. Gutmann, J. W. Zhang, X. Y. Zheng, Z. Y. Shan, N. Zhao, L. S. Wu, T. Shang P. Miao, T. Takabatake, M. Smidman , and H. Q. Yuan

Complex magnetic phase diagram in Ce₃Pd₆Sb₅ with a well-ordered superstructure

W. Xie,[1,2,3] M. Gutmann [®],[4] J. W. Zhang,[2] X. Y. Zheng,[2] Z. Y. Shan,[2] N. Zhao,[1,3] L. S. Wu,[5] T. Shang [®],[6] M. Smidman [®],[2,*]
P. Miao,[1,3] T. Takabatake [®],[7] and H. Q. Yuan[2,8,9,†]

[1]*Institute of High Energy Physics, Chinese Academy of Sciences, Beijing 100049, People's Republic of China*
[2]*Center for Correlated Matter and School of Physics, Zhejiang University, Hangzhou 310058, People's Republic of China*
[3]*Spallation Neutron Source Science Center, Dongguan 523803, People's Republic of China*
[4]*ISIS Facility, Rutherford Appleton Laboratory, Chilton, Didcot OX11 0QX, United Kingdom*
[5]*Department of Physics, Southern University of Science and Technology, Shenzhen 518055, People's Republic of China*
[6]*Key Laboratory of Polar Materials and Devices (MOE), School of Physics and Electronic Science,*
East China Normal University, Shanghai 200241, People's Republic of China
[7]*Department of Quantum Matter, Graduate School of Advanced Science and Engineering,*
Hiroshima University, Higashi-Hiroshima 739-8530, Japan
[8]*State Key Laboratory of Silicon and Advanced Semiconductor Materials, Zhejiang University, Hangzhou 310058, People's Republic of China*
[9]*Collaborative Innovation Center of Advanced Microstructures, Nanjing 210093, People's Republic of China*

We report multiple magnetic phase transitions in single-crystalline $Ce_3Pd_6Sb_5$ using magnetic, transport, and thermodynamic measurements. $Ce_3Pd_6Sb_5$ crystallizes in an orthorhombic structure (space group *Pmmn*), as a defect-induced variant of the well-known tetragonal $CaBe_2Ge_2$ structure. It undergoes two magnetic transitions: a second-order antiferromagnetic transition at $T_{N1} = 6.6$ K and a first-order one at $T_{N2} = 5.8$ K. The hybridization between $4f$ electrons and conduction electrons is relatively weak in $Ce_3Pd_6Sb_5$, as revealed from the nearly full recovery of magnetic entropy $R\ln2$ at T_{N1} and the low value of the electronic specific-heat coefficient of 30 mJ/(Ce-mol K²). We construct two field-temperature phase diagrams for magnetic fields applied parallel and perpendicular to the c axis, which, for $H \parallel c$, shows multiple field-induced phases between $T_{N1}(H)$ and $T_{N2}(H)$, while Hall resistivity measurements point to the absence of a topological Hall effect. The crystalline electric field effect and modulated crystalline structure with two Ce sites are considered as the primary factors for the complex magnetic properties of $Ce_3Pd_6Sb_5$.

I. INTRODUCTION

The competition and cooperation between itinerancy and localization of electrons are the main physical mechanisms behind the diverse physical states in many quantum material systems, which is well exemplified by Ce-based intermetallics [1–4]. The $4f^1$ electron configuration of Ce^{3+} can lead to both itinerancy and localization, which, on one hand, may hybridize with the conduction electrons resulting in the Kondo effect, while, on the other hand, it could remain a local moment forming long-range magnetic order as a consequence of the Ruderman-Kittel-Kasuya-Yosida (RKKY) interaction. The competition between the Kondo effect and RKKY magnetic interaction, as the physics behind the Doniach phase diagram, may lead to a quantum critical point with strong quantum fluctuations, where unconventional superconductivity, non-Fermi liquid, and other novel emergent phenomena usually appear [2,4–6].

Interesting physical properties may also emerge in weakly correlated Ce-based compounds with localized magnetism,

where different types of magnetic interactions interplay with crystalline electric fields (CEF) and spin-orbit coupling [7–9]. One example is CeAlGe with a polar noncentrosymmetric structure, where a topological nontrivial meron/anti-meron lattice magnetic structure has been discovered under magnetic fields, formed by the local moments [7].

$Ce_3Pd_6Sb_5$ is a Sb-deficient variant of $CePd_2Sb_2$ with the $CaBe_2Ge_2$-type structure, in which the defects are well ordered, leading to a superstructure with well-defined composition [10,11]. Different from $CePd_2Sb_2$, the body-centered sublattice formed by Ce ions in $Ce_3Pd_6Sb_5$ is largely distorted, which leads to two inequivalent Ce sites: Ce_1 and Ce_2, as shown in Fig. 1, as well as a lowering of the crystal symmetry from tetragonal to orthorhombic. The existence of two inequivalent Ce sites may result in unusual physical properties, such as potential competitive and/or cooperative Kondo screening effects [12], and complex magnetic properties related to different CEF ground states. So far, only limited physical properties measured on polycrystalline samples have been reported for $Ce_3Pd_6Sb_5$, which indicate an antiferromagnetic transition at 6.0 K [10]. In view of the various novel emergent phenomena discovered in the CeT_2X_2 (T = transition metal; X = p-block elements) intermetallics [13–15], it is rather interesting to characterize the physical properties of

---

(a)

(b)

(c)
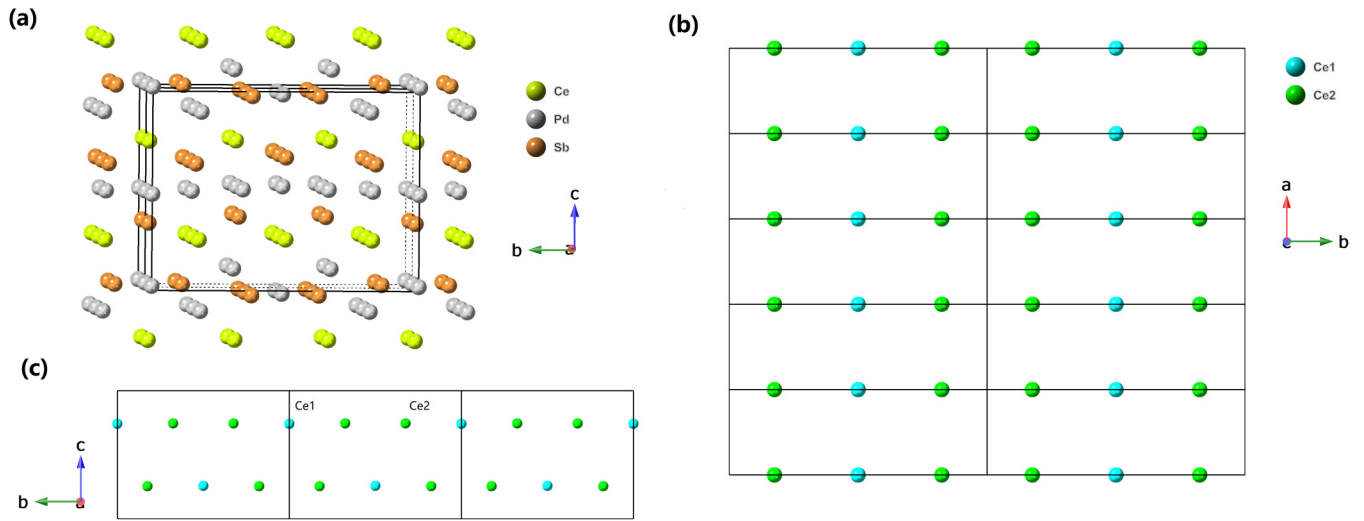

FIG. 1. Illustration of the crystal structure of $Ce_3Pd_6Sb_5$ along different directions. (a) The overall structure tilted slightly away from the a axis; (b) one layer of the Ce sublattice in the ab plane; (c) the Ce sublattice along the a axis. The Ce atoms at different Wyckoff sites are distinguished by using different colors in (b) and (c). Note that there are two identical layers of Ce atoms along the c axis in one unit cell with an in-plane shift of $(0.5a, 0.5b, 0)$ between them. The interplane distances along the c axis are, alternatively, 4.856 and 5.165 Å for Ce_1, and 4.916 and 5.105 Å for Ce_2. The neighboring Ce-Ce distances along the b axis are 4.372 Å for Ce_1-Ce_2 and 4.729 Å for Ce_2-Ce_2. The neighboring Ce-Ce distances along the a axis are 4.457 Å for both Ce_1-Ce_1 and Ce_2-Ce_2.

$Ce_3Pd_6Sb_5$ with a distorted $CaBe_2Ge_2$-type structure and two Ce sites.

Here, we report structural, magnetic, transport, and thermodynamic measurements of $Ce_3Pd_6Sb_5$ single crystals grown by a eutectic Pd-Sb flux, which reveal that $Ce_3Pd_6Sb_5$ undergoes two magnetic transitions at 6.6 and 5.8 K, being different from a single transition at 6.0 K reported on a polycrystalline sample [10]. By applying magnetic fields along the c axis, both T_{N1} and T_{N2} are suppressed to lower temperatures with three field-induced transitions between $T_{N1}(H)$ and $T_{N2}(H)$. We have constructed the H–T phase diagrams for fields applied parallel and perpendicular to the c axis.

II. EXPERIMENTAL METHODS

Single crystals of $Ce_3Pd_6Sb_5$ were grown using a flux method, where a eutectic Pd-Sb mixture with a molar ratio of 1:1 was used as a flux. Ce pieces (99.9%), Pd powder (99.95%), and Sb powder (99.999%) from Alfa Aesar were combined in an alumina crucible, which was sealed in an evacuated quartz ampule, slowly heated to $1000\,°C$ and kept there for one day before being cooled at a rate of $1.5\,°C/h$ to $750\,°C$, at which temperature the ampule was removed from the furnace and centrifuged. The centrifuged quartz ampule was put into the furnace again and annealed at $700\,°C$ for about two days. Platelike crystals with maximum dimensions of $1 \times 1 \times 0.5$ mm^3 were obtained.

The crystal structure was examined with a Rigaku-Oxford diffraction Xtalab synergy single-crystal diffractometer equipped with a HyPix hybrid pixel array detector using Mo-$K_{\alpha 1}$ radiation. The single-crystalline orientation and powder x-ray diffraction (XRD) were measured using a Rigaku Ultima IV diffractometer with Cu $K_{\alpha 1}$ radiation. The chemical composition was determined by energy-dispersive x-ray spectroscopy (EDS) using a Hitachi SU-8010 field emission

scanning electron microscope. The electrical resistivity, Hall resistivity, and heat capacity were measured using a Quantum Design Physical Property Measurement System (QD PPMS-9T) with a ^{3}He insert. The magnetic susceptibility and magnetization were measured down to 2 K using a Quantum Design Magnetic Property Measurement System (QD MPMS-5T) and a vibrating sample magnetometer on a Physical Property Measurement System (PPMS-14T).

III. RESULTS AND DISCUSSION

A. Crystal structure

An image of a single crystal is shown in the inset of Fig. 2. The average composition of the obtained single crystal determined via EDS is 3.00:6.14:5.14 for Ce:Pd:Sb, which is close to the stoichiometric $Ce_3Pd_6Sb_5$ composition. The main panel of Fig. 2 shows the XRD pattern measured on a piece of single crystal of $Ce_3Pd_6Sb_5$, in which the diffraction peak positions match well with the expected $(00l)(l = \text{integer})$ peak positions [10], indicating that the crystal surface is oriented perpendicular to the c axis. The phase purity of the crystals is further demonstrated by powder XRD measured on crushed single crystals, shown in Fig. 2. Results of the Rietveld refinement to the structure of $Ce_3Pd_6Sb_5$ show these are single phase with no observed unindexed impurity peaks.

Single-crystal XRD analysis on a crystal of about $100 \times 100 \times 80$ μm^3 confirmed the crystal structure of $Ce_3Pd_6Sb_5$, yielding lattice parameters of $a = 4.4568(1)$, $b = 13.4742(2)$, and $c = 10.020\,90(10)$ Å, which is well consistent with previous reports of orthorhombic $Ce_3Pd_6Sb_5$ [10]. The crystallographic data obtained from the Rietveld refinement on single-crystal XRD data are shown in Table I.

The crystal structure determined by single-crystal XRD measurements is shown in Fig. 1. As a superstructure variant of the $CaBe_2Ge_2$-type structure, the original body-centered

TABLE I. Crystallographic data of $Ce_3Pd_6Sb_5$ obtained from the Rietveld analysis of the single-crystal XRD data.

Crystal data							
Crystal family	Orthorhombic						
Space group (no.)	*Pmmn* (59)	Atoms	x	y	z	Occupancy	U_{iso}
a (Å)	4.4568(1)	Ce1	0	0.5	0.25770(5)	1	0.00537(12)
b (Å)	13.4742(2)	Ce2	0	0.175 50(3)	0.25471(4)	1	0.00475(9)
c (Å)	10.020 90(10)	Sb1	0	0.626 23(4)	−0.02303(5)	1	0.00751(11)
α, β, γ (deg)	90	Sb2	1	0.5	0.66947(7)	1	0.00813(15)
Unit-cell volume (Å^3)	601.773(11)	Sb3	0.5	0.663 37(3)	0.36313(5)	1	0.00640(11)
Rietveld refinement		Pd1	0.5	0.5	0.51610(8)	1	0.00929(18)
Computer program	JANA2006	Pd2	0.5	0.682 38(4)	0.10267(6)	1	0.01048(13)
R_1 ($I \geqslant 3\sigma$/all)	0.0291/0.0317	Pd3	−0.5	0.5	−0.02256(9)	1	0.01103(19)
$wR2$ ($I \geqslant 3\sigma$/all)	0.0792/0.0801	Pd4	1	0.66087(4)	0.50841(6)	1	0.00925(13)
S ($I \geqslant 3\sigma$/all)	2.21/2.18						

Ce sublattice distorts, in which case, the Ce_1 site is no longer body centered, and the lattice parameters a and b are no longer equal for the lattice formed by Ce_2. In another aspect, the Ce atoms form chains along the b axis, as shown in Fig. 1(b), where every Ce_1 atom is sandwiched by two Ce_2 atoms with distances $d(Ce_1\text{-}Ce_2) = 4.372$ Å and $d(Ce_2\text{-}Ce_2) = 4.729$ Å. The interchain distances along the a axis are all 4.457 Å,

forming Ce planes in the ab plane. Furthermore, the Ce_1 and Ce_2 layers are not exactly in the same plane with a small difference of 0.03 Å along the c axis, i.e., the Ce planes in the ab plane are buckled. The distances between the Ce_1 planes are alternatively 4.856 and 5.165 Å along the c axis, which are 4.916 and 5.105 Å between Ce_2 planes. Compared to the parent $CaBe_2Ge_2$-type structure, both the space-group symmetries and site symmetries for Ce ions in $Ce_3Pd_6Sb_5$ are largely reduced.

B. Low-field physical properties
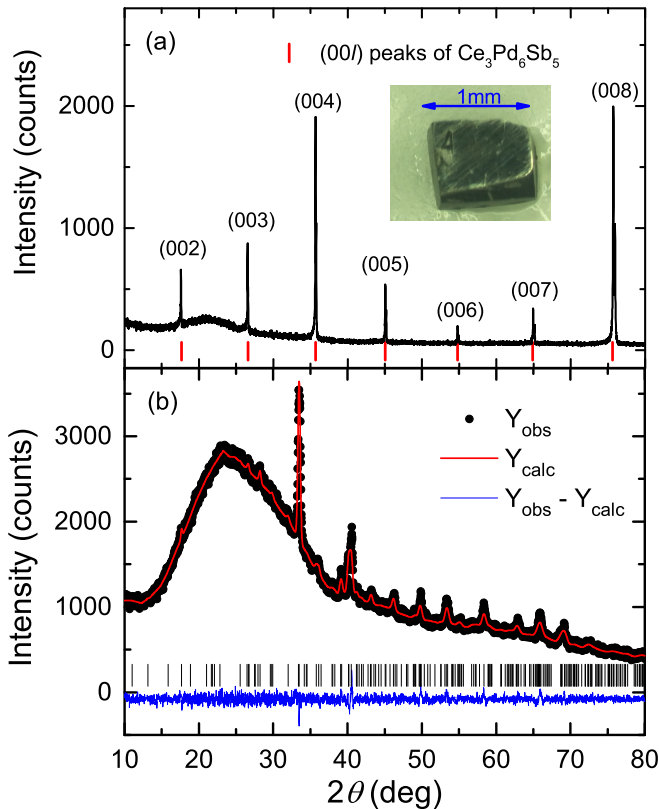
The temperature dependence of the electrical resistivity $\rho(T)$ with the current in the ab plane is shown in Fig. 3, which exhibits a negative curvature from 300 to 17 K. Below 17 K, $\rho(T)$ increases slightly, followed by a sharp decrease upon cooling below T_{N1} of 6.6 K. The residual resistivity ratio defined as $\rho(300\text{ K})/\rho(1.9\text{ K})$ is 23. Such a value indicates a well-ordered structure, and is about five times larger than that reported for polycrystalline samples [10]. The negative curvature at high temperatures and the low-temperature minimum could arise due to the Kondo effect, as well as the thermal
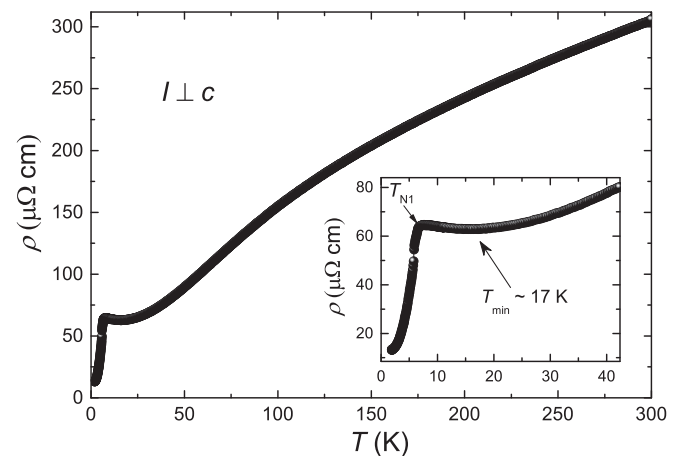

FIG. 2. (a) XRD pattern of a $Ce_3Pd_6Sb_5$ single crystal with a surface plane perpendicular to the c axis, measured with Cu $K_{\alpha1}$ radiation. Inset: A piece of single crystal with a typical length of 1.0 mm. (b) Powder XRD pattern of crushed single crystals of $Ce_3Pd_6Sb_5$, together with the Rietveld refinement calculation. Note that the broad hump centered around 25 degrees arises from the glass sample holder.

FIG. 3. Temperature dependence of the resistivity $\rho(T)$ of $Ce_3Pd_6Sb_5$ from 300 to 1.9 K, where the electric current was applied in the ab plane. Inset: An enlargement below 40 K, where a minimum is observed at about 17 K.
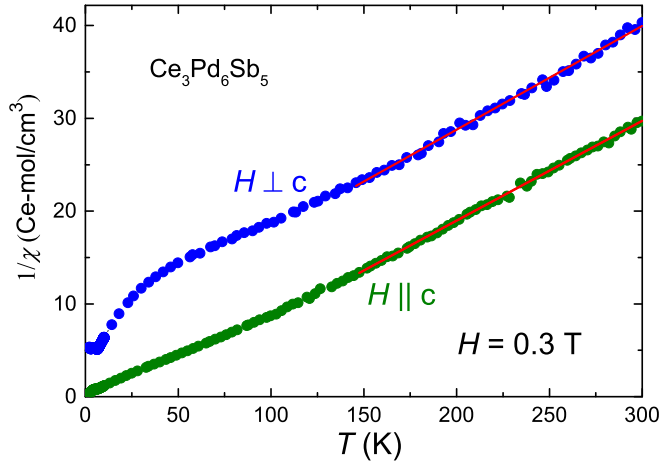
FIG. 4. Inverse magnetic susceptibility $1/\chi(T)$ of $Ce_3Pd_6Sb_5$ from 300 to 2 K for both $H \parallel c$ and $H \perp c$. The solid lines are fits to the high-temperature data with the Curie-Weiss law.

depopulation of excited CEF levels and enhanced magnetic scattering just above T_N [16].

In Fig. 4, the inverse magnetic susceptibility $1/\chi(T)$ from 300 to 2 K is shown for fields applied along two directions, $H \parallel c$ and $H \perp c$. The high-temperature behavior of $\chi(T)$ can be fitted by Curie-Weiss law $\chi = C/(T - \theta_P)$, while deviations occur upon cooling below 150 K. The effective moments μ_{eff} and Weiss temperature θ_P obtained from the Curie-Weiss fit are $2.43\mu_B$/Ce and 23.6 K for $H \parallel c$, respectively, $2.38\mu_B$/Ce and -56.5 K for $H \perp c$, respectively. The deviations at low temperatures could be either due to the effect of CEF or Kondo screening of local moments. Note that due to the low site symmetries for the two sites of the Ce ions, fitting $\chi(T)$ based on a model for the CEF Hamiltonian is largely overparameterized.

Figure 5 shows the low-temperature behavior of the electrical resistivity $\rho(T)$, specific heat $C(T)/T$, and $\chi(T)$, revealing two transitions at $T_{N1} = 6.6$ and $T_{N2} = 5.8$ K. Measuring resistivity upon warming up and cooling down showed a thermal hysteresis at T_{N2}, in contrast to a cusp at T_{N1} without a hysteresis, indicating a first-order transition at T_{N2} and a second-order transition at T_{N1}. The two transitions manifest more clearly in $C(T)/T$, as shown in Fig. 5(b), where a λ-like jump occurs at T_{N1} and there is a narrow sharp peak at T_{N2}. Below T_{N2}, $C(T)/T$ decreases linearly to tens of mJ/(Ce-mol K^2) and flattens below 1 K. Two transitions are also shown in $\chi(T)$, where a cusp and an abrupt drop are observed at T_{N1} and T_{N2}, respectively, indicating a magnetic origin of the two transitions. $\chi(T)$ measured upon warming after both zero-field cooling (zfc) and field cooling (fc) in a field of 0.5 T is shown in the inset of Fig. 5(b). No splitting of these curves is observed at either transition, consistent with them both being antiferromagnetic. Notably, $\chi(T)$ at T_{N1} for $H \parallel c$ is about six times larger than that for $H \perp c$, indicating a relatively large magnetic anisotropy in $Ce_3Pd_6Sb_5$. $\chi(T)$ decreases monotonically below T_{N1} and T_{N2} for $H \parallel c$, while it nearly flattens for $H \perp c$, which indicates that the ordered moments are parallel to the easy c axis. Extrapolation of the c-axis susceptibility $\chi_c(T)$ (between T_{N1} and T_{N2}) down to zero temperature gives
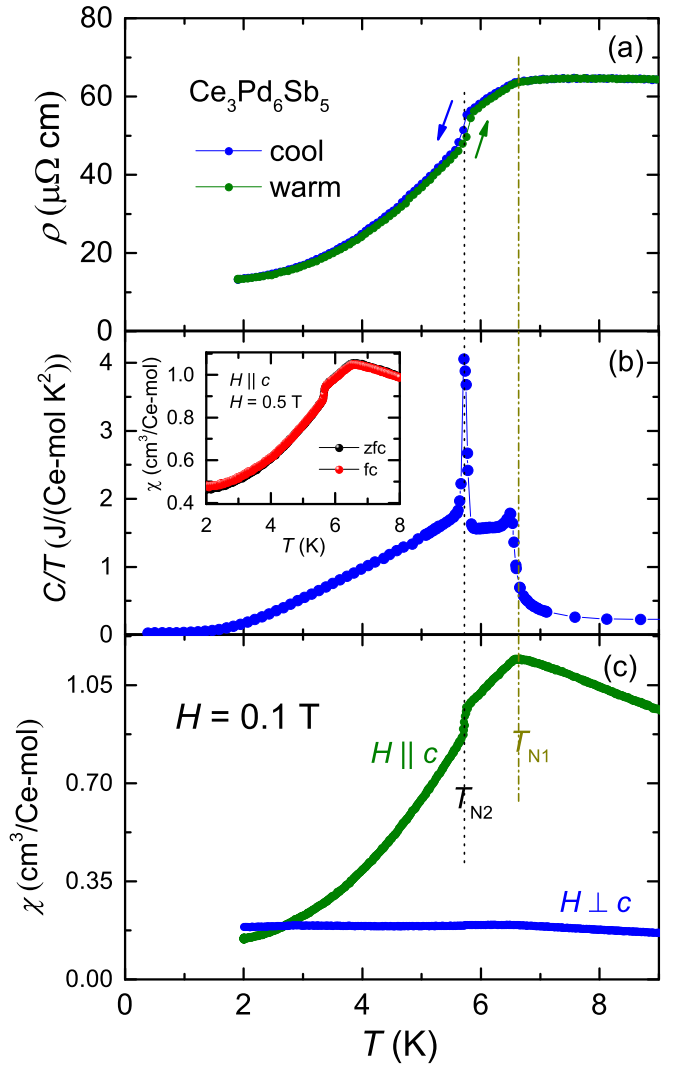

FIG. 5. Temperature dependence of (a) resistivity $\rho(T)$ measured with the electric current in the ab plane, (b) specific heat as $C(T)/T$ in zero magnetic field, and (c) magnetic susceptibility $\chi(T)$ measured in a magnetic field of 0.1 T applied parallel and perpendicular to the c axis. The inset of (b) shows the low-temperature magnetic susceptibility $\chi(T)$ measured upon warming, after cooling with zero magnetic field cooling (zfc) and field cooling (fc) in 0.5 T.

a nearly zero value, consistent with a collinear antiferromagnetic structure with ordered moments along the c axis [17]. The slope is almost the same above and below T_{N2} in $\chi_c(T)$, suggesting a subtle change in the magnetic structure upon cooling across T_{N2}.

The T^2 dependence of the specific heat as $C(T)/T$ is shown in the main panel of Fig. 6, which is fitted using $C/T = \gamma + \beta T^2$. The obtained β of 1.32 mJ/(Ce-mol K^4) is used for the calculation of the phonon contribution to C/T below 10 K, which is then subtracted from the C/T data. The $4f$ electronic contribution $C_{4f}(T)/T$ is plotted in the inset. The C_{4f}/T data flatten below 1 K, leading to a Sommerfeld coefficient γ of 30 mJ/(Ce-mol K^2). Such a small γ value compared with typical heavy-fermion Ce-based compounds indicates a weak Kondo effect in $Ce_3Pd_6Sb_5$. Furthermore, the magnetic entropy ΔS is calculated by inte-
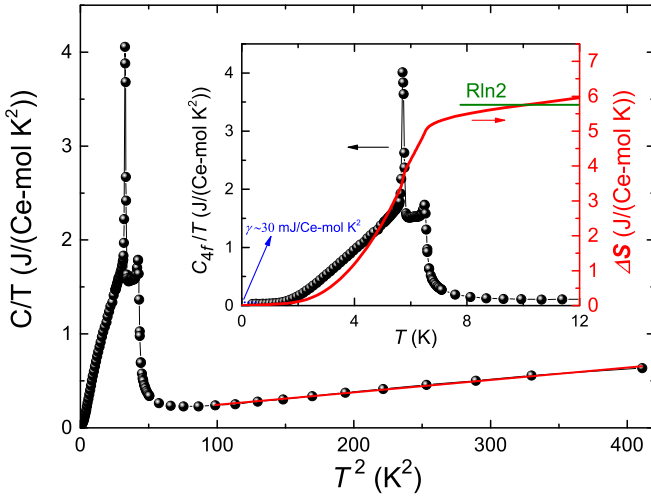
FIG. 6. Specific heat as C/T vs T^2, where the red line indicates a linear fit. Inset: C_{4f}/T together with the magnetic entropy ΔS obtained by integrating C_{4f}/T with respect to T from 0.3 K.

grating C_{4f}/T from the lowest measured temperature 0.3 K (the negligible contribution below 0.3 K is ignored). As can be seen in the inset of Fig. 6, ΔS of $0.91R\ln2$ is recovered at $T_{N1} = 6.6$ K. Consistent with the small γ value, this evidences a weak Kondo effect in $Ce_3Pd_6Sb_5$.

C. Physical properties under magnetic fields

Figures 7(a) and 7(b) show $M(T)/H$ for various magnetic fields applied along the c axis and ab plane, respectively. With increasing field, both T_{N1} and T_{N2} are suppressed to lower temperature, as shown by the black and blue arrows, respectively. The cusp at T_{N1} becomes increasingly sharper at higher fields, where a drop is observed right below T_{N1} of increasingly larger size. At T_{N2}, on the other hand, the thermal loop becomes larger with increasing magnetic field. Furthermore, three field-induced magnetic transitions are observed, as shown by the red, cyan, and magenta arrows. All the field-induced transitions display thermal loops for which the loop sizes increase with magnetic field. $M(T)/H$ gradually flattens below T_{N1} with increasing magnetic field. In contrast to the strong effect of $H \parallel c$, $M(T)/H$ for $H \perp c$ shows little change. As can be seen in Fig. 7(b), both T_{N1} and T_{N2} only decrease by about 0.5 K in fields up to 9 T.

The isothermal magnetization $M(H)$ is shown in Fig. 8, where field-induced transitions for $H \parallel c$ are resolved. No transitions occur for $H \perp c$ up to 9 T. On the contrary, five jumps and one kink are present in $M(H)$ for $H \parallel c$ at 2 K, corresponding to five transitions and one crossover to the field-induced polarized (FP) state, where magnetic hysteresis is observed for the four transitions in $M(H)$, indicating four first-order transitions on the low-field side ($H \leqslant 5$ T). The fifth jump without hysteresis corresponds to $T_{N1}(H)$. The saturated moment at 2.1 K is about $1.47\,\mu_B$/Ce, which is comparable to the saturated moment of a CEF doublet ground state of $|m_J = 3/2 >$, $1.28\,\mu_B$/Ce. However, due to the large number of free parameters in the CEF Hamiltonian, the exact ground state is difficult to determine based on present measurements. The $M(H)$ for $H \perp c$ increases linearly with field,
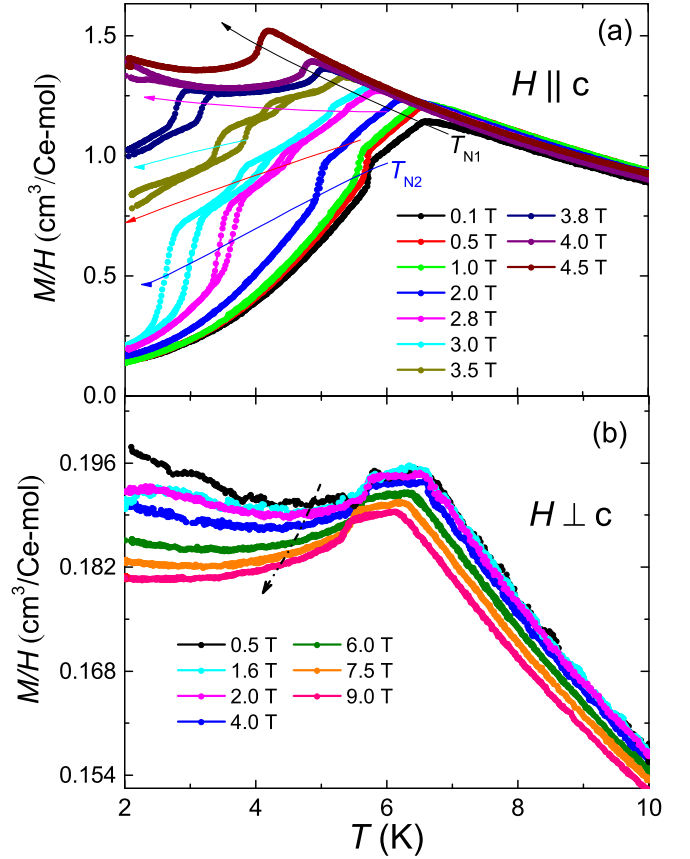

FIG. 7. $M(T)/H$ under various constant magnetic fields up to 9 T applied (a) parallel and (b) perpendicular to the c axis. The arrows with different colors are used to show the evolution of the different transitions with applied magnetic fields: the black arrow denotes T_{N1}; blue denotes T_{N2}; the red, cyan, and magenta arrows denote the field-induced transitions T_{FIT1}, T_{FIT2}, and T_{FIT3}, respectively.

where the moment at 9 T is six times smaller than that for $H \parallel c$. The large difference in magnetization between $H \parallel c$ and $H \perp c$ further reveals the sizable uniaxial magnetocrystalline anisotropy in $Ce_3Pd_6Sb_5$.

The resistivity under applied magnetic fields $\rho(T, H)$ was also measured up to 9 T. As shown in Fig. 9(a), for $H \parallel c$, the cusp and discontinuity in $\rho(T)$ at zero field, corresponding to T_{N1} and T_{N2}, respectively, remain in magnetic fields up to 3 T. Thereafter, only a broad kink is observed in $\rho(T)$, which should be assigned to T_{N1}. The kink can no longer be resolved for fields higher than 5 T, where a broad hump shows up and shifts to higher temperature with increasing magnetic field. The field-induced increase of the hump temperature could be due to the crossover to the field-induced ferromagnetic state. The resistivity upturn above T_{N1} is gradually suppressed and changes into a decrease. This change can be resolved more readily from the $\rho(H)$ data shown in Fig. 10(a). Above T_{N1}, $\rho(H)$ decreases monotonically, indicating the suppression of spin-flip scattering by magnetic fields. At 6 K, a kink corresponding to T_{N1} is observed. Upon cooling, at 5.5 K, hysteresis between field-up and field-down sweeps begins to emerge, in addition to the kink at higher field, which is due to the first-order transition at T_{N2}. Upon further cooling, additional
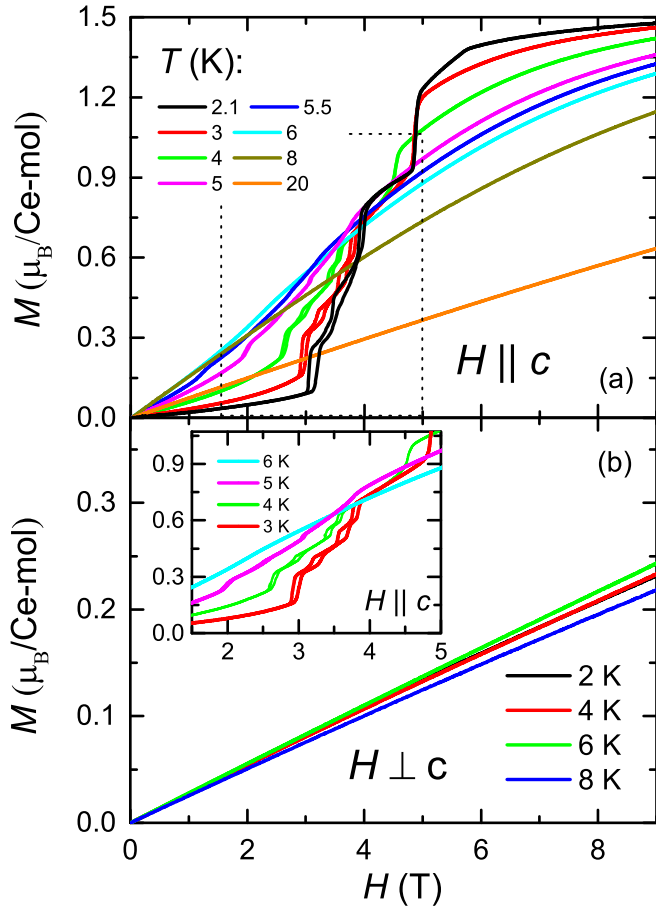
FIG. 8. Isothermal magnetization $M(H)$ measured at several temperatures for (a) $H \parallel c$ and (b) $H \perp c$. The inset of (b) enlarges the range in the dotted square in (a).
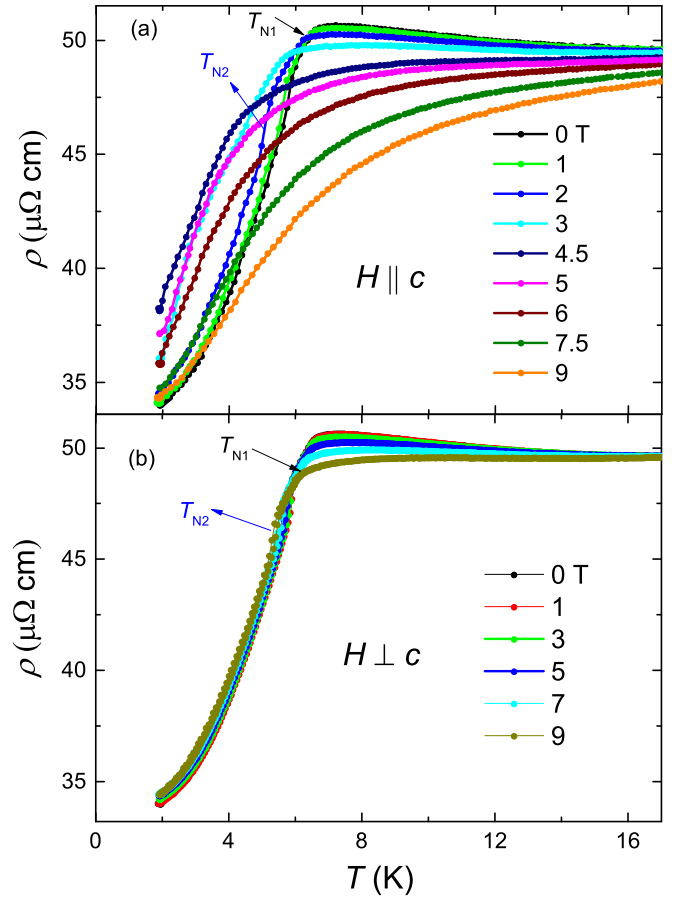

FIG. 9. Temperature dependence of the resistivity $\rho(T)$ measured in various magnetic fields up to 9 T for (a) $H \parallel c$ and (b) $H \perp c$, respectively.

anomalies appear in $\rho(H)$ for $H \parallel c$, where sizable hysteresis is observed in the field range of 2 and 4 T at 1.9 K. Note that in Fig. 10(a), the cusps at (4.5 K, 4.2 T) and (4 K, 4.4 T), and the drops at (3 K, 4.8 T) and (1.9 K, 4.9 T), are all related to the continuously suppressed T_{N1}.

Increasing the magnetic field has a relatively weak effect on $\rho(T, H)$ for $H \perp c$. As shown in Fig. 9(b), the cusp and discontinuity at T_{N1} and T_{N2}, respectively, remain similar to those in zero field, and below T_{N2}, $\rho(T)$ under different fields falls on one curve. As shown in Fig. 10(b), the largest MR occurs at 8 K, right above T_{N1}, in addition to a transition at (5.5 K, 7 T), which corresponds to T_{N2}.

D. Anisotropic $H-T$ phase diagram

We constructed the $H-T$ phase diagrams for $H \parallel c$ and $H \perp c$ by tracing the transition points in both $M(T, H)$ and $\rho(T, H)$. For $M(T)$, $M(H)$, and $\rho(T)$, the positions of the local maxima or the midpoints of the abrupt jumps in the derivative are taken as the transition points [see inset of Fig. 11(b)], while for $\rho(H)$, the midpoints of the jumps are used [see Fig. 10(a)]. As shown in Fig. 11, transition points from the different measurements coincide well with each other.

The phase diagram for $H \parallel c$ is much more complex than that for $H \perp c$, where three metamagnetic transitions are observed for $H \parallel c$, which are all situated between $T_{N1}(H)$ and $T_{N2}(H)$. The multiple metamagnetic transitions are likely a consequence of the uniaxial anisotropy with the easy direction along the c axis.

Whether the two magnetic transitions are caused by the sequential orderings of moments at Ce_1 and Ce_2 sites is an interesting question. However, our data indicate that this may not be the case since the $\chi(T)$ data show almost the same temperature dependence above and below T_{N2}, which points to a subtle change in magnetic structure upon cooling across T_{N2}, rather than a new ordering of the moments on a different Ce site. Moreover, the field dependences of the $M(H)$ curves at 5.0, 5.5, and 6.0 K (below and above T_{N2}) exhibit slight and gradual changes, evidencing magnetic order states arising from all Ce ions below both T_{N1} and T_{N2}. Such a picture is also consistent with the Ce sublattice in crystal structure, where the neighboring distance between Ce_1 and Ce_2 is shortest in the ab plane, indicating a relatively strong coupling between them.

E. Hall resistivity measurements

In view of the rather complex phase diagram for $H \parallel c$, Hall resistivity measurements were performed so as to look
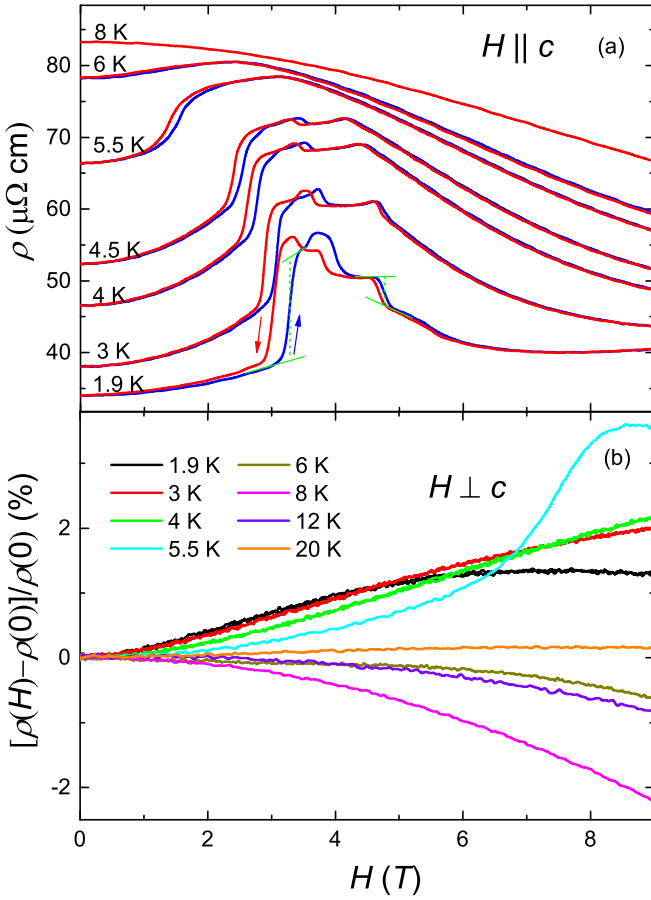
FIG. 10. (a),(b) Field dependence of the electrical resistivity for $H \parallel c$ and $H \perp c$, respectively. To see clearly the variation for $H \perp c$, the magnetoresistance $[\rho(H) - \rho(0)]/\rho(0)$ is shown in (b), instead of $\rho(H)$. The blue and red lines in (a) denote increasing field and decreasing field, respectively. The solid and dashed green lines illustrate the construction used to determine the midpoints of the jumps, taken as the positions of the transitions.

for a topological Hall effect (THE) that is characteristic of a potential topological spin texture, as observed in some rare-earth intermetallics with localized f electrons [7,18–20]. As shown in Fig. 12, at 2 K, a hump occurs starting from 3 T, which shifts to lower field with increasing temperature and finally disappears at 6 K. The deviations from linear behavior begin exactly at the field where the $M(H)$ curves exhibit the first transition. Furthermore, a distinct kink appears at higher field for both the 2, 3, and 4 K data, where the $M(H)$ curves start to saturate at H_{sat}. These observations indicate that the Hall resistivity are closely related to the magnetization, suggesting a contribution of the anomalous Hall effect (AHE).

Generally, the anomalous Hall resistivity ρ_{xy}^A can be proportional to either M, $\rho_{xx}M$, or $\rho_{xx}^2 M$, depending on the particular mechanism [21]. Together with the normal contribution, the Hall resistivity in ordinary magnetic systems has a form of $\rho_{xy} = \rho_{xy}^N + \rho_{xy}^A$, where ρ_{xy}^A is a term proportional to the magnetization. However, in topological systems (or magnetic system with nonzero spin chirality), an additional contribution may add to the total Hall resistivity, which cannot be described by the above expressions, i.e., THE [21]. In a
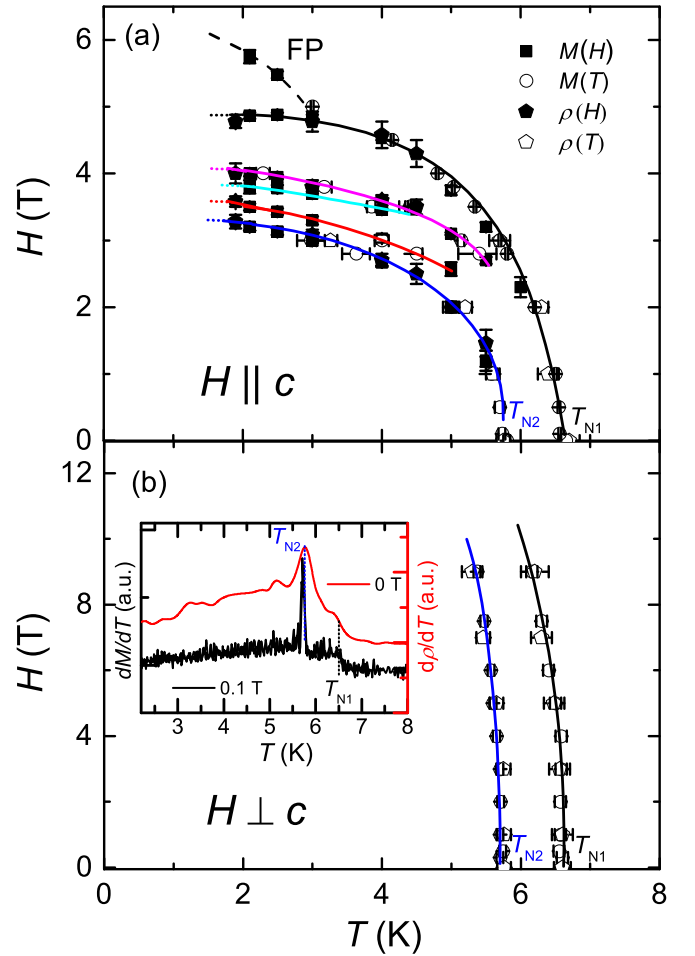

FIG. 11. T–H phase diagrams for (a) $H \parallel c$ and (b) $H \perp c$ of $Ce_3Pd_6Sb_5$, constructed from measurements of $M(T, H)$ and $\rho(T, H)$. The solid lines are a guide to the eye, while the colors correspond to the arrows labeling the evolution of the transitions in Fig. 7. The dashed line in (a) shows the crossover where $M(H)$ starts to saturate. The error bars correspond to the transition widths, which were defined as the corresponding full width at half maximum of the peaks in the derivative, or the width of the jumps used to determine the transition points. The inset of (b) shows the derivatives of $M(T)$ and $\rho(T)$ used to determine the transition positions in the phase diagram.

two-band model, the Hall resistivity is described by

$$\rho_{xy}^N = \frac{H}{e} \frac{(n_h \mu_h^2 - n_e \mu_e^2) + (n_h - n_e)(\mu_e \mu_h)^2 H^2}{(n_h \mu_h + n_e \mu_e)^2 + (n_h - n_e)^2 (\mu_e \mu_h)^2 H^2}, \quad (1)$$

where n_e and n_h are the carrier concentrations of electrons and holes, respectively, while μ_e and μ_h are the respective mobilities [22].

For $Ce_3Pd_6Sb_5$, the $\rho_{xy}(H)$ data below 6 K show an obvious decrease above H_{sat}, while both $M(H)$ and ρ_{xx} flatten or even slightly increase above H_{sat}, indicating a nonlinear ρ_{xy}^N in $Ce_3Pd_6Sb_5$ at low temperature. This is further evidenced by the nonlinear ρ_{xy} at 10 K ($> T_{N1}$). In Fig. 12, we show the fits using the above equations, where a two-band normal Hall contribution [Eq. (1)], and an anomalous Hall contribution of
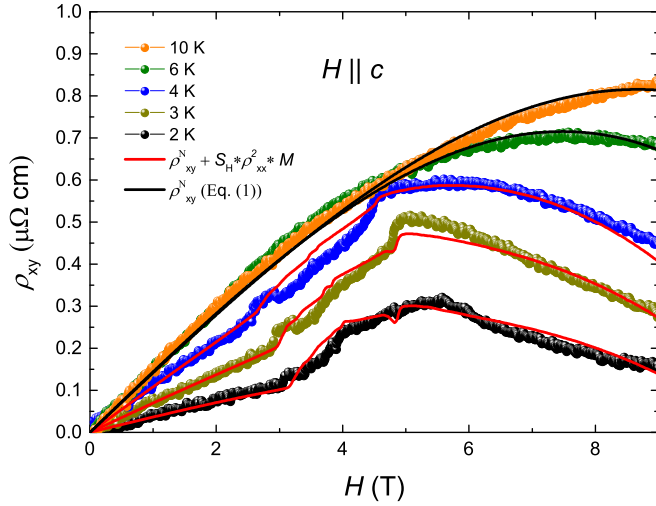
FIG. 12. Isothermal field dependence of the Hall resistivity for $H \parallel c$. The solid lines show that the model fits using the equations given in the main text.

the form of $S_H \rho_{xx}^2 M$ which fits the data best, are displayed. The fit parameters are listed in Table II.

It can be seen that this model can reasonably well account for the main features of the experimental data. Note that since there are five experimental parameters, the fitting parameters are unlikely to be unique, but the analysis shows that the data can be fitted by such a model and therefore there is a lack of a clear THE. Note again that a THE generally manifests as a hump in the Hall resistivity that cannot be described by the above equations [7,18,20].

Recently, magnetic-order-induced AHE and THE have been reported in several Eu-based compounds [23–25]. In both $EuCd_2As_2$ and $EuZn_2Sb_2$, $\rho_{xy}(H)$ shows linear behavior at high magnetic fields, indicating a single-band behavior for the normal contribution, making it easy to subtract $\rho_{xy}^N(H)$ [23,24]. In $EuAl_4$, a humplike anomaly is also observed in $\rho_{xy}(H)$ below the magnetic ordering temperature [25]. However, due to the two-band normal contribution, three possible scenarios were considered for the AHE to separate the different contributions, i.e., $\rho_{xy}^A(H)$ proportional to either M, $\rho_{xx}M$, or $\rho_{xx}^2 M$. Since none of these scenarios could account for this anomaly, it was concluded that it indeed arose from a THE. In contrast to $EuAl_4$, a model taking into account the normal and AHE contributions could describe the data of $Ce_3Pd_6Sb_5$. Note that here we first fitted the two-band normal contribution, where, due to overparameterization, it was necessary to constrain the parameters in Eq. (1) to reasonable values based on the measured longitudinal resistivity (ρ) of

the order of $\mu\Omega$ cm and the small MR. In comparison, for semimetallic YbAs, $\rho(T)$ is of a similar magnitude, while a large MR is observed due to the large mobilities and compensated semimetal nature with rather small Fermi pockets ($n_e = n_h$) [26]. The carrier densities for YbAs were determined to be about 4.7×10^{26} m^{-3} and the carrier mobilities up to 4–6 m^2 V^{-1} s^{-1} at 2 K [26].

IV. SUMMARY

In summary, we have synthesized single crystals of $Ce_3Pd_6Sb_5$ and confirmed the well-ordered orthorhombic superstructure. Two magnetic transitions are observed with a second-order antiferromagnetic (AFM) transition at $T_{N1} = 6.6$ K and a first-order one at $T_{N2} = 5.8$ K. The phase diagrams for magnetic fields both parallel and perpendicular to the c axis are constructed, where both T_{N1} and T_{N2} are continuously suppressed by fields, while the rate of suppression for $H \perp c$ is much smaller than that for $H \parallel c$. Three field-induced transitions are observed for $H \parallel c$ between $T_{N1}(H)$ and $T_{N2}(H)$, while no field-induced transition is observed for $H \perp c$. The analysis of the Hall resistivity points to the absence of a THE, suggesting that the magnetic structure under magnetic fields is most likely topologically trivial.

Our measurements indicate that the Kondo effect in $Ce_3Pd_6Sb_5$ is relatively weak, and the CEF effects of the two sites of Ce^{3+} ions under low site symmetries are responsible for most of the experimental observations. It would be interesting to determine the magnetic structures by using neutron and resonant x-ray scattering techniques, which may give more insights into the magnetic properties of compounds with multiple magnetic sites and low crystalline symmetry.

TABLE II. Fitting parameters obtained from analysis of the Hall resistivity at different temperatures.

	n_h ($\times 10^{26}$ m^{-3})	n_e ($\times 10^{26}$ m^{-3})	μ_h (m^{2}V^{-1} s^{-1})	μ_e (m^{2}V^{-1} s^{-1})	S_H [mol(μ_B $\mu\Omega$ cm)$^{-1}$]
2 K	20.00	22.60	0.45	0.250	0.35
3 K	20.00	22.59	0.71	0.255	0.31
4 K	20.00	22.60	1.40	0.250	0.31
6 K	20.00	22.45	6.50	0.215	
10 K	20.00	21.88	5.00	0.213	

[1] G. R. Stewart, Heavy-fermion systems, Rev. Mod. Phys. **56**, 755 (1984).

[2] C. Pfleiderer, Superconducting phases of f-electron compounds, Rev. Mod. Phys. **81**, 1551 (2009).

[3] F. Steglich and S. Wirth, Foundations of heavy-fermion superconductivity: Lattice Kondo effect and Mott physics, Rep. Prog. Phys. **79**, 084502 (2016).

[4] Z. F. Weng, M. Smidman, L. Jiao, X. Lu and H. Q. Yuan, Multiple quantum phase transitions and superconductivity in Ce-based heavy fermions, Rep. Prog. Phys. **79**, 094503 (2016).

[5] G. R. Stewart, Non-Fermi-liquid behavior in d- and f-electron metals, Rev. Mod. Phys. **73**, 797 (2001).

[6] P. Gegenwart, Q. Si, and F. Steglich, Quantum criticality in heavy-fermion metals, Nat. Phys. **4**, 186 (2008).

[7] P. Puphal, V. Pomjakushin, N. Kanazawa, V. Ukleev, D. J. Gawryluk, J. Ma, M. Naamneh, N. C. Plumb, L. Keller, R. Cubitt, E. Pomjakushina, and J. S. White, Topological magnetic phase in the candidate Weyl semimetal CeAlGe, Phys. Rev. Lett. **124**, 017202 (2020).

[8] B. K. Rai, J. Banda, M. Stavinoha, R. Borth, D.-J. Jang, K. A. Benavides, D. A. Sokolov, J. Y. Chan, M. Nicklas, M. Brando, C.-L. Huang, and E. Morosan, $CeIr_3Ge_7$: A local moment antiferromagnetic metal with extremely low ordering temperature, Phys. Rev. B **98**, 195119 (2018).

[9] Y. Kawaue, R. Oishi, C. Yang, R. Yamamoto, Y. Shimura, K. Umeo, T. Onimaru, D. T. Adroja, H. C. Walker, and T. Takabatake, Weak Kondo coupling antiferromagnet $CePd_3Sn_2$ with quasi-one-dimensional Ce chains, J. Phys. Soc. Jpn. **93**, 034706 (2024).

[10] R. A. Gordon, F. J. DiSalvo, R. Pöttgen, Crystal structure and physical properties of $Ce_3Pd_6Sb_5$, J. Alloys Compd. **228**, 16 (1995).

[11] I. Schellenberg, R.-D. Hoffmann, S. Seidel, C. Schwickert, and R. Pöttgen, Magnetic properties of $RE_3Pd_6Sb_5$ (RE = Pr, Nd, Gd) and a group-subgroup scheme for $Ce_3Pd_6Sb_5$ and $Yb_5Cu_{11}Sn_8$, Z. Naturforsch. B **66**, 1179 (2011).

[12] A. Benlagra, L. Fritz, and M. Vojta, Kondo lattices with inequivalent local moments: Competitive versus cooperative Kondo screening, Phys. Rev. B **84**, 075126 (2011).

[13] F. Steglich, J. Aarts, C. D. Bredl, W. Lieke, D. Meschede, W. Franz, and H. Schafer, Superconductivity in the presence of strong Pauli paramagnetism: $CeCu_2Si_2$, Phys. Rev. Lett. **43**, 1892 (1979).

[14] T. T. M. Palstra, A. A. Menovsky, G. J. Nieuwenhuys, and J. A. Mydosh, Magnetic properties of the ternary compounds CeT_2Si_2 and UT_2Si_2, J. Magn. Magn. Mater. **54–57**, 435 (1986).

[15] T. Endstra, G. J. Nieuwenhuys, and J. A. Mydosh, Hybridization model for the magnetic-ordering behavior of uranium-and cerium-based 1:2:2 intermetallic compounds, Phys. Rev. B **48**, 9595 (1993).

[16] M. O. Ajeesh, T. Shang, W. B. Jiang, W. Xie, R. D. dos Reis, M. Smidman, C. Geibel, H. Q. Yuan, and M. Nicklas, Ising-type magnetic anisotropy in $CePd_2As_2$, Sci. Rep. **7**, 7338 (2017).

[17] V. K. Anand and D. C. Johnston, Metallic behavior induced by potassium doping of the trigonal antiferromagnetic insulator $EuMn_2As_2$, Phys. Rev. B **94**, 014431 (2016).

[18] R. Takagi, N. Matsuyama, V. Ukleev, L. Yu, J. S. White, S. Francoual, J. R. L. Mardegan, S. Hayami, H. Saito, K. Kaneko, Y. Ōnuki, T. Arima, Y. Tokura, T. Nakajima, and S. Seki, Square and rhombic lattices of magnetic skyrmions in a centrosymmetric binary compound, Nat. Commun. **13**, 1472 (2022).

[19] T. Kurumaji, T. Nakajima, M. Hirschberger, A. Kikkawa, Y. Yamasaki, H. Sagayama, H. Nakao, Y. Taguchi, T. Arima, and Y. Tokura, Skyrmion lattice with a giant topological Hall effect in a frustrated triangular-lattice magnet, Science **365**, 914 (2019).

[20] M. Kakihana, D. Aoki, A. Nakamura, F. Honda, M. Nakashima, Y. Amako, S. Nakamura, T. Sakakibara, M. Hedo, T. Nakama, and Y. Ōnuki, Giant Hall resistivity and magnetoresistance in cubic chiral antiferromagnet EuPtSi, J. Phys. Soc. Jpn. **87**, 023701 (2018).

[21] N. Nagaosa, J. Sinova, S. Onoda, A. H. MacDonald, and N. P. Ong, Anomalous Hall effect, Rev. Mod. Phys. **82**, 1539 (2010).

[22] J. M. Ziman, *Electrons and Phonons: The Theory of Transport Phenomena in Solids* (Oxford University Press, Oxford, UK, 2001).

[23] Y. Xu, L. Das, J. Z. Ma, C. J. Yi, S. M. Nie, Y. G. Shi, A. Tiwari, S. S. Tsirkin, T. Neupert, M. Medarde, M. Shi, J. Chang, and T. Shang, Unconventional transverse transport above and below the magnetic transition temperature in Weyl semimetal $EuCd_2As_2$, Phys. Rev. Lett. **126**, 076602 (2021).

[24] K. Singh, O. Pavlosiuk, S. Dan, D. Kaczorowski, and P. Wiśniewski, Large unconventional anomalous Hall effect arising from spin chirality within domain walls of an antiferromagnet $EuZn_2Sb_2$, Phys. Rev. B **109**, 125107 (2024).

[25] T. Shang, Y. Xu, D. J. Gawryluk, J. Z. Ma, T. Shiroka, M. Shi, and E. Pomjakushina, Anomalous Hall resistivity and possible topological Hall effect in the $EuAl_4$ antiferromagnet, Phys. Rev. B **103**, L020405 (2021).

[26] W. Xie, Y. Wu, F. Du, A. Wang, H. Su, Y. Chen, Z. Y. Nie, S.-K. Mo, M. Smidman, C. Cao, Y. Liu, T. Takabatake, and H. Q. Yuan, Magnetotransport and electronic structure of the antiferromagnetic semimetal YbAs, Phys. Rev. B **101**, 085132 (2020).